Computers and Fluids 227 (2021) 105032

Contents lists available at ScienceDirect

Computers and Fluids

journal homepage: www.elsevier.com/locate/compfluid

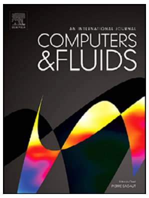

A sharp interface immersed boundary method for flow-induced noise prediction using acoustic perturbation equations

Cheng Zhao[a,c], Yan Yang[b,c], Tao Zhang[a,*], Haibo Dong[c], Guoxiang Hou[a]

[a] School of Naval Architecture & Ocean Engineering, Huazhong University of Science & Technology, Wuhan, Hubei 430074, China
[b] LHD, Institute of Mechanics, Chinese Academy of Sciences, Beijing 100190, China
[c] Department of Mechanical and Aerospace Engineering, University of Virginia, Charlottesville, VA 22904, USA

ARTICLE INFO

Article history:
Received 23 June 2020
Revised 5 April 2021
Accepted 26 May 2021
Available online 31 May 2021

Keywords:
Acoustic perturbation equations
Immersed boundary method
Flow-induced noise
Four-cylinder array

ABSTRACT

In this paper, a hybrid computational aero/hydro-acoustic approach is proposed to deal with acoustic scattering and flow-induced noise problems based on the sharp interface immersed boundary method (IBM). For the flow field, the incompressible Navier–Stokes equations are solved by an in-house direct numerical simulation solver. The acoustic field is predicted by solving acoustic perturbation equations (APEs). Both flow and acoustic solid boundaries with complexity and mobility are dealt with by the sharp interface IBM. Benchmark acoustic problems with varied scatterers in two and three dimensions are presented to validate the accuracy of the acoustic codes and boundary treatments. Then, the feasibility and accuracy of the present hybrid approach are validated by considering the problem of flow past a circular cylinder at a Reynolds number of 200. Subsequently, the present method is used to predict the noise generated by flow around a four-cylinder array in two-dimensions with two arrangements (i.e., square array and diamond array), and the flow and acoustic physics are investigated in detail. The results show that the square array retains a monopole-like sound-radiation shape, while the directivity pattern of the diamond array produces a dipole-like shape. In both the square and diamond arrays, the propagation of acoustic waves is affected by the Doppler effect, and the latter array results in a larger alternation of the propagation angle compared with the single cylinder due to the influence of the geometric configuration. The intensity of the radiated acoustic pressure is much greater for the diamond array compared to the square one in most circumferential directions, and the acoustic intensity of both arrays is greater than that of the single cylinder. The spectrums of the far-field acoustic pressure indicate that the two arrays and the single cylinder have similar peak frequencies and profiles, with vortex shedding playing the predominant role in noise generation in all three configurations.

© 2021 Published by Elsevier Ltd.

1. Introduction

Studies on sound generation and propagation by unsteady flow are important in practical applications such as jet noise, marine propellers, and turbomachinery. Recently, much research has been conducted on the fluid dynamics inspired by fast and efficient propulsion [1-4], due to the great potential of applications in biomimetics. However, research on noise prediction has not received adequate attention. Investigations of flow-induced noise play an important role in the design of quiet drones and bio-inspired robots. Besides, underwater acoustic propagation can also be applied in underwater navigation systems and ocean depth measurement.

In previous studies, theoretical methods [5,6], experimental measurements [7,8], and numerical simulations [9-19] have been used to investigate acoustic scattering and flow-induced noise problems. Compared with the former two methods, numerical simulation has particular advantages in multiple aspects, such as parametric studies and mechanism research. Numerical techniques for acoustic simulation include direct numerical simulation (DNS) [11,14,18] and a hybrid method; the latter is widely applied due to the high cost of DNS [20]. In the hybrid approach, the acoustic field is decoupled from the flow field and is solved by deriving acoustic governing equations. The hybrid method can be mainly classed into the acoustic analogy method [15], linearized Euler Equations (LEEs) [13,21], and the hydrodynamic/acoustic splitting approach [9,10,22,23]. Compared with the acoustic analogy method, the other two methods can obtain the noise source and can consider the convection as well as refraction effects of the non-uniform flow

---

[*] Corresponding author.
E-mail address: zhangt7666@hust.edu.cn (T. Zhang).

https://doi.org/10.1016/j.compfluid.2021.105032
0045-7930/© 2021 Published by Elsevier Ltd.

on the acoustic field, which is more suitable for the mechanism analysis of sound generation and propagation.

Previously, Hardin and Pope [9] proposed an acoustic/viscous splitting technique for the numerical analysis of aerodynamic noise generation, and the approach was validated by sound generation in a two-dimensional cavity. Additionally, Bailly and Juve [21] studied acoustic propagation problems by solving LEEs with various source terms and compared them with analytical solutions to check the accuracy of the numerical simulations. To suppress the instability of LEEs due to entropy and vorticity waves, Ewert and Schröder [10] formulated a family of acoustic perturbation equations (APEs) for the simulation of flow-induced acoustic fields and used this method to predict the trailing edge noise [24]. Seo and Moon [12] studied low-Mach number flow-induced sound by solving linearized perturbed compressible equations (LPCEs) and validated the method for various dipole and quadruple vortex-sound problems.

As demonstrated by the aforementioned references, research on acoustic problems has seen renewed activity in recent years. However, one challenge for acoustic simulation is the boundary treatment, especially for complex and moving boundaries. The use of an unstructured grid or an overset grid are two methods that can be applied to deal with this condition. However, unstructured grid is difficult to extend to high-order accuracy. Overset grid method consists of two non-coincident grids in the overlap region and the coupling between them is accomplished using interpolation. However, the generation of the overset grid and the data exchange is still very complicated for complex geometry. An important method to deal with complex geometry and moving boundary problems in computational fluid dynamics (CFD) is the immersed boundary method (IBM), which has been successfully applied to solve many bio-inspired problems [25-28]. For acoustic problems, Seo and Mittal [29] studied acoustic wave scattering and low-Mach number flow-induced sound by solving LPCEs with a high-order IBM based on a weighted least-squares error method, and this method was then applied to study the effect of wing flexibility on sound generation [30]. However, when the ghost point is close to the immersed boundary, a scenario may occur in which most of the interpolation points are covered by the solid itself. Under this condition, the radius of the local support region must be increased to ensure a sufficient number of fluid points; thus, the interpolation efficiency may be lost, and even leading to numerical instabilities during the interpolation process [31]. Fukushima et al. [32] developed a LEE solver using a block-structured Cartesian mesh to address complex geometry and validated the acoustic scattering around a sphere, and subsequently applied the method to compute the noise propagation from the JT15D nacelle; however, the acoustic sources were artificial. Dhamankar et al. [33] implemented a similar ghost-point-based sharp IBM via a compressible large eddy simulation (LES) method to simulate jet aeroacoustics; however, this method has a weakness in that it has a high computational cost and is hard to apply on very low-Mach number problems such as underwater acoustics.

To the authors' knowledge, no study has ever combined APEs with IBM. Though the equations of APEs are similar to those of LEEs, the APE system can render stable solutions even in flows where hydrodynamic instabilities are present by suppressing entropy and vorticity waves. Besides, the APE system is very efficient comparing with LPCEs as the velocity vector is constant in time. However, the instantaneous flow velocity must be updated for LPCEs, which leads to additional computational requirements. For flow-induced noise problem, the expression of acoustic source for LPCEs are also more complicated than those of APEs. The source term of LPCEs is the substantial time derivative of the pressure [12] for vortex sound problems, while the dominant source term of APEs is given by the spatial derivative of the perturbation pressure [10]. In terms of the IBM, the boundary conditions on the immersed surface can be precisely satisfied at the actual location, which allows for a sharp representation of the immersed boundary. Besides, the interpolation efficiency and numerical instability can be retained even for complex geometries. The primary contribution of the present work is that it presents a unique combination of APEs with immersed boundary treatment and uses numerical implementation to simulate acoustic scattering and flow-induced noise problems. The APE system is solved by optimized computational aeroacoustic (CAA) numerical schemes and techniques, with acoustic sources imported from the flow field, which is obtained from the CFD solver. The sharp interface IBM is used in both the CFD and CAA solvers. Benchmark two- and three-dimensional problems in acoustic scattering are shown in order to test the present acoustic codes. Subsequently, the sound generation by a two-dimensional circular cylinder in a uniform flow is computed. Finally, the flow and acoustic field of flow past a four-cylinder array in two different arrangements are investigated in detail.

2. Computational method

2.1. Governing equations

In this paper, a hybrid method is applied to simulate the flow and acoustic field. The flow field is first simulated to obtain the acoustic sources, and then the acoustic field is computed by solving acoustic equations. The governing equations for fluid flow are the incompressible Navier–Stokes (NS) equations, which can be written in vector form as follows:

$$\nabla \cdot \boldsymbol{u} = 0 \tag{1}$$

$$\frac{\partial \boldsymbol{u}}{\partial t} + (\boldsymbol{u} \cdot \nabla)\boldsymbol{u} = -\frac{1}{\rho_0}\nabla P + \nu_0 \nabla^2 \boldsymbol{u} \tag{2}$$

where ρ_0, $\boldsymbol{u}$, and P are the incompressible flow density, velocity vector, and pressure, respectively. ν_0 is the kinematic viscosity of the fluid. The non-slip, adiabatic wall boundary conditions are used on the solid wall for the incompressible NS equations, which can be expressed as follows:

$$\frac{\partial P}{\partial n} = 0, \ \ \boldsymbol{u} = 0 \tag{3}$$

The propagation of acoustic waves in a non-uniform flow is usually calculated using the LEEs. This accounts for the effects of both refraction and convection caused by the non-uniform mean flow. However, LEEs also support the propagation of vorticity and entropy waves. If the entropy or vorticity modes are excited by the source terms, especially in flows where hydrodynamic instabilities are present, the LEEs can return unstable solutions.

In order to remove hydrodynamic instabilities and obtain stable solutions, Ewert and Schröder [10] reformulated the wave propagation model by assuming that the acoustic field is irrotational and isentropic such that vorticity and entropy modes no longer appear, and they obtained a system of APEs for the acoustic modes only. The equations of APEs are excited by source terms determined from the simulation of the compressible or incompressible flow problem.

The equations of APEs can be derived by decomposing the primitive perturbation variables into a time-averaged part and a fluctuating part as follows [10]:

$$\begin{aligned} &\rho(\mathbf{x},t) = \bar{\rho}(\mathbf{x},t) + \rho'(\mathbf{x},t), \\ &\mathbf{u}(\mathbf{x},t) = \bar{\mathbf{u}}(\mathbf{x},t) + \mathbf{u}'(\mathbf{x},t) = \bar{\mathbf{u}}(\mathbf{x},t) + \mathbf{u}^{\mathrm{v}}(\mathbf{x},t) + \mathbf{u}^{\mathrm{a}}(\mathbf{x},t), \\ &p(\mathbf{x},t) = \bar{p}(\mathbf{x},t) + p'(\mathbf{x},t), \\ &h(\mathbf{x},t) = \bar{h}(\mathbf{x},t) + h'(\mathbf{x},t) \end{aligned} \tag{4}$$

where p is the pressure, ρ is the density, $\boldsymbol{u}$ is the velocity, h is the enthalpy, primed quantities denote perturbation quantities, the bar symbol denotes time-averaged quantities, $\boldsymbol{u}^{\mathrm{v}}$ is a solenoidal vortical perturbation, and $\boldsymbol{u}^{\mathrm{a}}$ is an irrotational acoustic perturbation. The continuity equation and momentum equation written with the enthalpy h and the velocities $\boldsymbol{u}$ as variables can be expressed as follows [10]:

$$\frac{\partial \rho}{\partial t} + \nabla . (\rho \mathbf{u}) = 0 \tag{5}$$

$$\frac{\partial \mathbf{u}}{\partial t} + \nabla h = -(\mathbf{u} . \nabla)\mathbf{u} + \frac{\nabla . \underline{\tau}}{\rho} + T\nabla s \tag{6}$$

where T is the temperature, s is the entropy, and the stress tensor is denoted by $\underline{\tau}$. Take equations (4) into Eqs. (5) and (6) and neglect the non-linear acoustic terms. In the continuity equation, the perturbation density is replaced by the perturbation pressure via the first-order form of the second law of thermodynamics. In the momentum equations, assume an irrotational acoustic perturbation velocity, i.e., $\boldsymbol{\omega}^a = \nabla \times \boldsymbol{u}^{\mathrm{a}} = 0$, and substitute the perturbation pressure for the perturbation enthalpy using the second law of thermodynamics. Then, the complete system of APEs can be written in vector form as follows [10]:

$$\frac{\partial p'}{\partial t} + \bar{c}^2 \nabla . (\bar{\rho}\mathbf{u}^{\mathrm{a}} + \bar{\mathbf{u}}\frac{p'}{\bar{c}^2}) = \bar{c}^2 S_{\mathrm{cont}} \tag{7}$$

$$\frac{\partial \mathbf{u}^{\mathrm{a}}}{\partial t} + \nabla(\bar{\mathbf{u}} . \mathbf{u}^{\mathrm{a}}) + \nabla(\frac{p'}{\bar{\rho}}) = \mathbf{S}_{\mathrm{mom}} \tag{8}$$

with sources

$$S_{\mathrm{cont}} = \underbrace{-\nabla \rho \cdot \mathbf{u}^{\mathrm{v}}}_{I} + \underbrace{\frac{\bar{\rho}}{c_{\mathrm{p}}} \frac{\bar{D}s'}{Dt}}_{II} \tag{9}$$

$$\mathbf{S}_{\mathrm{mom}} = \underbrace{\nabla \Phi_{\mathrm{p}}}_{III} + \underbrace{\nabla q_{\bar{\omega}}}_{IV} + \underbrace{T' \nabla \bar{s} - s' \nabla \bar{T}}_{V} \tag{10}$$

where $\bar{D}/Dt = \partial/\partial t + \bar{\mathbf{u}} . \nabla$ denotes the substantial time derivative, and terms III and IV follow

$$\nabla^2 \Phi_{\mathrm{P}} = -\nabla . \left[\frac{\partial \mathbf{u}^{\mathrm{v}}}{\partial t} + (\bar{\mathbf{u}} . \nabla)\mathbf{u}^{\mathrm{v}} + (\mathbf{u}^{\mathrm{v}} . \nabla)\bar{\mathbf{u}} + ((\mathbf{u}^{\mathrm{v}} . \nabla)\mathbf{u}^{\mathrm{v}})' - \left(\frac{\nabla . \underline{\tau}}{\rho} \right)' \right] \tag{11}$$

$$\nabla^2 q_{\omega} = -\nabla . (\bar{\omega} \times \mathbf{u}^{\mathrm{a}}) \tag{12}$$

The left-hand sides of APEs describe the wave propagation and refraction in a non-uniform mean flow. The right-hand terms S_{cont} and $\boldsymbol{S}_{\mathrm{mom}}$ are acoustic sources in the continuity and momentum equations, respectively.

The source terms I and III are functions of the solenoidal perturbation velocity $\boldsymbol{u}^{\mathrm{v}}$, while the terms II and V involve entropy and temperature fluctuations, respectively. If combustion noise is not considered, these two terms are discarded. Furthermore, in the low-Mach number limit, $\rho \to \rho_0$ and $\nabla \rho \to 0$ hold such that source term I drops. Term IV describes sound generation due to acoustic/mean–vorticity interaction, which can be negligible for external flow problems [10]. For vortex sound, term III is the major source term, which is determined by the solution of the Poisson problem. As can be seen from the terms in brackets on the right-hand side of Eq. (11) for small Mach numbers, the Φ_{P} is equal to P'/ρ_0, where $P' = P - \bar{P}$ is the incompressible perturbation pressure, and ρ_0 is the constant mean flow density. Term III can be evaluated by the following equation:

$$\nabla \Phi_{\mathrm{p}} \simeq \frac{\nabla P'}{\rho_0} = \frac{\nabla \left(P - \bar{P}\right)}{\rho_0} \tag{13}$$

As the flow is assumed to be inviscid for acoustic simulation, the slip boundary conditions are used on the solid wall. These can be expressed as follows:

$$\frac{\partial \rho'}{\partial n} = 0, \; \frac{\partial p'}{\partial n} = 0, \; \boldsymbol{u}' \cdot \boldsymbol{n} = 0 \tag{14}$$

where $\boldsymbol{n}$ is the unit wall-normal vector, and the initial conditions are $\rho' = 0, \; \boldsymbol{u}' = 0$, and $p\prime = p'_0$.

2.2. Numerical methodology

A second-order central difference based on a sharp interface IBM solver [25] is employed to solve the incompressible Navier–Stokes equations. The equations are discretized in space by a second-order central difference scheme and integrated in time using the fractional step method. The convective terms and diffusion terms are performed with an Adams–Bashforth scheme and an implicit Crank–Nicolson scheme, respectively. This method can provide second-order accuracy in both space and time and has been successfully applied for solving bio-inspired problems with complex geometry and moving boundaries [26-28].

In acoustic simulations, the acoustic waves are non-dispersive and non-dissipative in propagation, which can be achieved by high-order finite-difference schemes. The standard way to create such schemes is to use a Taylor series truncation to obtain the maximum possible order of accuracy. However, this type of central difference scheme is not constructed from a dispersive perspective. Tam and Webb [34] constructed a seven-point fourth-order dispersion relation preserving (DRP) scheme based on a minimalization of the dissipation and dispersion errors. The Runge–Kutta (RK) scheme is the most commonly used type of high-order time scheme. Hu et al. [35] optimized the coefficients of the RK scheme and proposed a low-dissipation and low-dispersion Runge–Kutta (LDDRK) scheme to minimize the dissipation and dispersion errors. For a symmetric stencil, the first derivative of DRP scheme can be written on the uniform mesh as follows:

$$\frac{\partial f}{\partial x}(x_0) \simeq \frac{1}{\Delta x} \sum_{j=-3}^{3} a_j f(x_0 + j\Delta x) \tag{15}$$

where a_j are the coefficients listed in Table 1 [34,36].

Near the solid boundary, a standard central difference scheme is applied. At the first fluid nodes adjacent to the solid boundary (see Fig. 1), the second-order central difference scheme is used, whereas the second fluid nodes adjacent to the solid boundary are computed by the fourth-order central difference scheme. At the domain boundary, backward difference stencils [36] are applied.

The spatial derivative of the non-uniform Cartesian grid can be evaluated by the following transformation:

$$\frac{\partial f}{\partial x} = \frac{\partial \xi}{\partial x}\frac{\partial f}{\partial \xi} = \frac{1}{\partial x/\partial \xi}\frac{\partial f}{\partial \xi} \tag{16}$$

where ξ is an arbitrary uniform grid. The spatial derivative at the mth grid point yields

$$\frac{\partial f}{\partial x}(x_m) \simeq \frac{1}{\widetilde{\Delta} x} \sum_{j=-3}^{3} a_j f_{m+j}, \text{with} \widetilde{\Delta} x = \sum_{j=-3}^{3} a_j x_{m+j} \tag{17}$$

As the metric, $\partial\xi/\partial x = 1/(\partial x/\partial \xi)$, is also computed with the high-order DRP schemes, the order of accuracy can be retained. A similar transformation was also used by Bogey and Bailly [37].

The time evolution equation can be written as follows:

$$\frac{\partial U}{\partial t} = F(U) \tag{18}$$

Table 1
Coefficients of the dispersion relation preserving scheme ($a_{-j} = -a_j$).

a_0	a_1	a_2	a_3
0	0.77088238051822552	−0.166705904414580469	0.02084314277031176

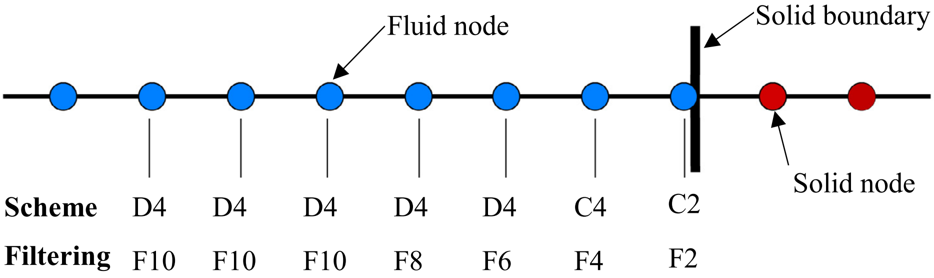

Fig. 1. Schematic of the numerical scheme and filtering on the Cartesian nodes.

Table 2
Coefficients of the six-stage low-dissipation and low-dispersion Runge–Kutta scheme.

β_1	β_2	β_3	β_4	β_5	β_6
0.169193539	0.1874412	1/4	1/3	1/2	1

An explicit six-stage LDDRK from the nth to the $(n+1)$th iterations is given as follows:

$$\begin{aligned} &U^0 = U^n \\ &U^l = U^n + \beta_l \Delta t F(U^{l-1}) \text{for} l = 1, \ldots, 6 \\ &U^{n+1} = U^6 \end{aligned} \tag{19}$$

where the values of β_l are as listed in Table 2 [35].

When a central finite difference scheme was used to approximate the spatial derivative, the wave number of the finite difference scheme was related to the actual wave number. The long waves behave like the corresponding wave component of the exact solution. However, the short waves have different propagation characteristics such that the wave number of the finite difference scheme differs from the true wave number. Therefore, the short waves, which can be generated by discontinuous initial conditions, are numerical contaminants of a computed solution. These short waves can cause spurious high-frequency oscillations and can lead to instabilities. To eliminate the grid-to-grid oscillations and maintain numerical stability, 10th-order spatial filtering [37] is applied at every iteration, and reduced-order spatial filtering (8th-, 6th-, 4th-, and 2nd-order) is used near the boundaries [38]. Applying a central, 2 N +1 point stencil filter provides:

$$D_f(x) = \sigma_d \sum_{j=-N}^{N} d_j f(x_0 + j\Delta x) \tag{20}$$

where d_j are the coefficients shown in Table 3, and σ_d is a constant between 0 and 1.

The numerical scheme and spatial filtering of the grids are presented in Fig. 1. The DRP scheme, central difference scheme, and filtering are denoted by “Dn”, “Cn”, and “Fn”, respectively, and “n” is the order of the scheme and filtering.

As the computational domain is finite in the simulation, a special treatment must be applied at the domain boundary to suppress numerical reflection. In this paper, the radiation conditions proposed by Tam and Dong [39], and developed for 3D by Bogey and Bailly [40], are used. The far-field equations are solved in boundary regions, three ghost nodes are constructed outside the physical domain, and backward DRP schemes are applied on these nodes.

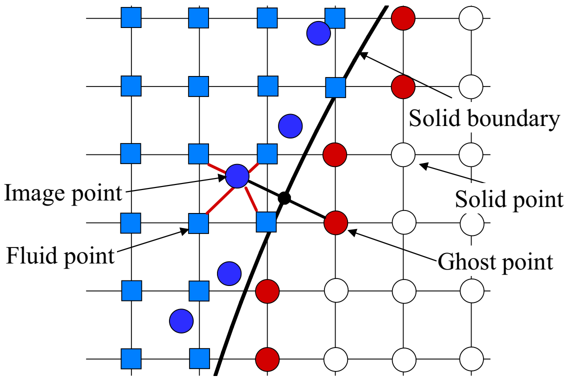

Fig. 2. Schematic of the solid boundary treatment.

2.3. Immersed boundary treatment

In this paper, both flow-field and acoustic-field boundaries use the immersed boundary treatment based on ghost points [25]. The treatment is described as follows. Firstly, the domain points are classified as fluid points, solid points, and ghost points, respectively. The solid points are the points inside the solid body, the fluid points are those outside the body, and the ghost points are the points that are inside the solid body but with at least one neighboring fluid point. Then, a line segment is extended from the ghost point to the fluid point that intersects normally with the solid boundary. The position of the image point is defined such that the boundary intercept is midway between the ghost point and the image point, as shown in Fig. 2. The variables on the image point (φ_{IP}) are then computed by bilinear/trilinear interpolation from surrounding fluid nodes, namely,

$$\varphi_{\mathrm{IP}} = \sum \beta_i \varphi_i \tag{21}$$

where β_i are the interpolation weights of the surrounding nodes. Once the value at the image point is obtained, the value of a variable at the ghost point is computed by using a central-difference approximation along the normal probe such that the prescribed boundary condition at the boundary intercept is incorporated. Thus, the formulae for Dirichlet and Neumann boundary conditions are:

$$\begin{aligned} &\varphi_{\mathrm{GC}} = 2\varphi_{\mathrm{BI}} - \varphi_{\mathrm{IP}} \\ &\text{and} \varphi_{\mathrm{GC}} = \varphi_{\mathrm{IP}} + \Delta l \left(\tfrac{\delta \varphi}{\delta n}\right)_{\mathrm{BI}} \end{aligned} \tag{22}$$

Table 3
Coefficients of the filters ($d_{-j} = d_j$).

	d_0	d_1	d_2	d_3	d_4	d_5
10th-order	63/256	−105/512	15/128	−45/1024	5/512	−1/1024
8th-order	35/128	−7/32	7/64	−1/32	1/256	
6th-order	5/16	−15/64	3/32	−1/64		
4th-order	3/8	−1/4	1/16			
2nd-order	1/2	−1/4				

respectively, where φ is the value of a generic variable and Δl is the length of the normal line segment extending from the ghost point to the image point. The subscripts 'GC', 'IP', and 'BI' represent the ghost point, image point, and body intercept point, respectively. Using this procedure, a second-order accuracy can be ensured for the boundary conditions in the computations [25].

3. Results and discussion

In this section, to test the present method and boundary treatment, the Gaussian pulse wave propagation and several benchmark problems in acoustic scattering are first considered and compared with analytical solutions. Subsequently, the noise induced by flow past a circular cylinder is validated. Then, the current method is applied to simulate the acoustic field of flow past a four-cylinder array with two configurations. In this section, the acoustic equations are non-dimensionalized by reference length l, the speed of sound c_0, and the ambient density ρ_0. Therefore, the time and pressure are non-dimensionalized with l/c_0 and $\rho_0 c_0^2$, unless specified in context.

3.1. Acoustic propagation of a Gaussian pulse

In this case, the propagation of a two-dimensional Gaussian pulse in a uniform mean flow ($Ma = 0.5$) [41] is computed to test the numerical schemes and the far-field non-reflecting boundary conditions. The computational domain is $-50 \le (x, y) \le 50$, and an artificial acoustic pulse is put in the center of the domain $x = y = 0$ with initial conditions as follows:

$$p' = \exp\left[-(ln2)\frac{x^2 + y^2}{3^2}\right], u' = v' = 0 \tag{23}$$

The APEs are solved on a 100 × 100 uniform mesh with $dx = dy = 1.0$ and CFL-number 0.75. The LEEs are also solved to compare with APEs. The instantaneous pressure contours and pressure perturbations along $y = 0$ at $t = 30$ and 50 are presented in Fig. 3. The results show that the pulse propagates in all directions at a velocity equal to the sum of the speed of sound and the flow velocity. When the wave arrives at the domain boundary, the pulse leaves the computational domain without noticeable reflections. Both pressure perturbations of APEs and LEEs along $y = 0$ at the corresponding time agree well with the analytical solutions, indicating that the numerical schemes and radiation boundary conditions are appropriate.

The uniform grids with $dx = dy = 1.0$, 0.5, 0.25, and 0.125 are used to test the grid convergence. The time step is set as 0.005 to minimize the effects of time on the solution. The $L1$, $L2$, and Linf norms of the error are calculated as follows:

$$L1 = \frac{1}{N}\sum_{n=1}^{N}\left|p'^{ana}_n - p'^{num}_n\right|, L2 = \sqrt{\frac{1}{N}\sum_{n=1}^{N}\left(p'^{ana}_n - p'^{num}_n\right)^2}, L\inf = \max_{1\le n\le N}\left|p'^{ana}_n - p'^{num}_n\right| \tag{24}$$

where p'^{ana}_n and p'^{num}_n are the analytical and numerical pressure perturbations at point n, and N is the number of grids. Three kinds of error at $t = 30$ are presented in Fig. 4(a). The results show that all the convergence rates of the simulations are about 4.0, which is the order of the DRP scheme. Besides, the root mean squares (RMSs) of the acoustic pressures for all grid points at different times are computed and compared with analytical solutions [41], as presented in Fig. 4(b). When the acoustic wave leaves the computation domain at about $t = 150$, the RMSs of the numerical simulations and analytical solutions are still in good agreement, showing that the present far-field radiation boundary conditions are suitable for acoustic radiation.

3.2. Acoustic wave scattering by a circular cylinder

In order to test the acoustic immersed boundary treatment, the acoustic wave scattering by a rigid circular cylinder (Fig. 5) [42] is simulated. A cylinder with diameter $D = 1$ is placed in the center of domain (0, 0). The acoustic source is a Gaussian pulse at (4, 0) with the following initial conditions:

$$p' = \exp\left[-(ln2)\frac{(x-4)^2 + y^2}{0.2^2}\right], u' = v' = 0 \tag{25}$$

The computational domain is $-6.0 \le (x, y) \le 6.0$, the uniform grid with $dx = dy = 0.02$ is used, and the CFL number is set to 0.5. The time histories of pressure fluctuation at four points, namely A ($x = 2$, $y = 0$), B ($x = 2$, $y = 2$), C ($x = 0$, $y = 2$), and D ($x = -2$, $y = 0$), are recorded and compared with the analytical solutions. The pressure fluctuation contours at different times are presented in Fig. 6. As shown in the figure, the wave propagates towards the boundaries, and the waves that are reflected from the right surface of the cylinder propagate towards the right boundary. The front wave deflects at the left surface of the cylinder. The sound pressures at four positions from $t = 0$ to $t = 10$ are shown in Fig. 7; good agreements can be observed between the simulation results and analytical solutions, indicating that the present immersed boundary treatment is effective and accurate.

The uniform grids with $dx = dy = 0.08$, 0.04, 0.02, and 0.01 are used to test the grid convergence including immersed boundary. The $L1$, $L2$, and Linf norms of the error are presented in Fig. 8. The results show that the convergence rates of the simulations are about 2.3, which is lower than those in the DRP scheme due to the lower-order treatments of the boundary conditions on the solid surface.

The second problem is the same as previous cylinder scattering problem except that the acoustic source is defined by a time harmonic Gaussian monopole source on the right hand of Eq. (7) as follows:

$$S_{\text{cont}} = \exp\left[-(ln2)\frac{(x-4)^2 + y^2}{0.2^2}\right] \cdot \sin(8\pi t) \tag{26}$$

In order to test non-uniform grids with acoustic scattering problems, stretched grids are used. A fine uniform grid with $dx = dy = 0.005$ is applied near the solid boundary, and the grid stretching ratio is set as 1.005. The maximum grid size is 0.032 at the domain boundary; this corresponds to about 7.8 points per wavelength (PPW), which is slightly higher than the grid resolution of the DRP scheme [34]. The total number of grids is 990 × 990 and the domain size is about $-6.1 \le (x, y) \le 6.1$. A uniform

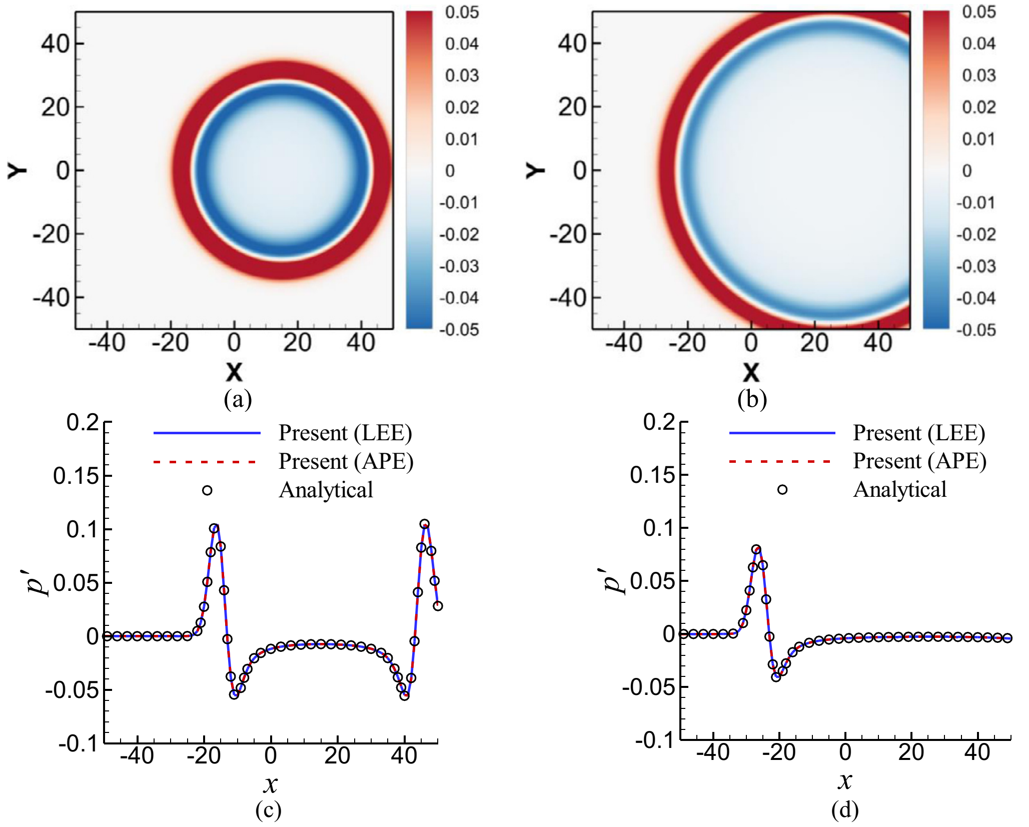

Fig. 3. Pressure perturbation contours at (a) $t = 30$, (b) $t = 50$ and the corresponding pressure perturbation along y axis at (c) $t = 30$, (d) $t = 50$.

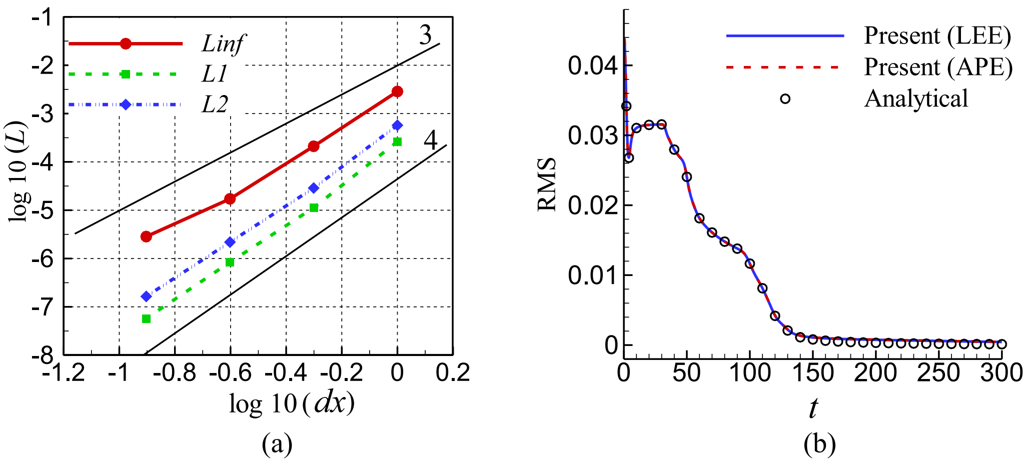

Fig. 4. (a) Convergence curve of pressure perturbation. (b) RMS of the acoustic pressure for all grid points from $t = 0$ to $t = 300$.

Cartesian grid with $dx = dy = 0.01$ (1200×1200) is also computed to compare the results. The pressure perturbation contour at time $t = 42$ is presented in Fig. 9(a) (uniform grid), while the directivity patterns, which are the RMSs of acoustic pressure in the time-periodic state, at $r = 0.55$ and $r = 5.0$ for uniform/non-uniform grids are plotted along with the analytical solution [42] in Figs. 9(b) and 9(c), respectively. In general, both the uniform grid and the non-uniform grid correspond well with the analytical solutions at $r = 0.55$ (near the boundary) and $r = 5.0$. However, in most numerical simulations, more grids are needed near the solid boundary to offset the reduced order and interpolation error, especially for a complex structure. The uniform grid significantly increases the total number of grids; thus, the non-uniform stretching grid is more effective and has better potential for dealing with complex geometry problems.

3.3. Acoustic wave scattering by a sphere

In this subsection, to test the numerical method for dealing with three-dimensional problems, the acoustic wave scattering by a stationary sphere [29,32,43] is simulated. A sphere with diameter $D = 1$ is placed at the coordinate origin (0, 0, 0), and a periodic monopole Gaussian source is given as follows:

$$S_{\text{cont}} = \exp\left[-(ln2)\frac{(x-4)^2+y^2+z^2}{0.2^2}\right]\cdot \sin(6\pi t) \tag{27}$$

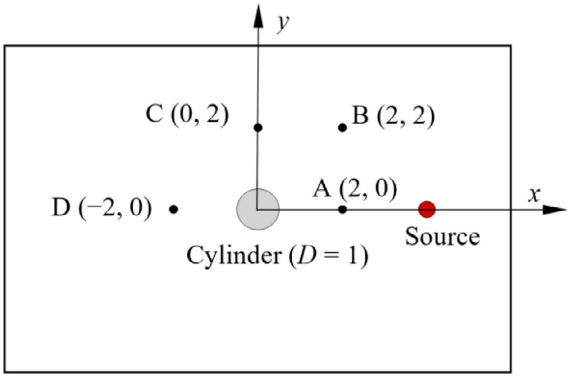

Fig. 5. Schematic position of acoustic scattering by a cylinder.

In order to minimize the computational cost, a set of non-uniform Cartesian grids is applied in this case. The uniform grid is still used in the center of the domain to capture the solid boundary, and the stretching mesh is used away from the solid. Note that the maximum grid size should be smaller than the acoustic resolution limit, which means that there must be at least 6–8 PPW for the DRP scheme. For this case, the minimum uniform grid size near the boundary is 0.012 and the stretching ratio is 1.02. In order to maintain the accuracy of the DRP scheme, the uniform grid is used when the grid size reaches 0.04, which is about 8.3 PPW. The total number of grids is 430 × 280 × 280 and the computation domain is about $-6.4 \le x \le 6.4$, $-3.2 \le (y, z) \le 3.2$. The time step is set as 0.006. A snapshot of the pressure perturbation field at $t = 24$ and the directivity pattern at $r = 2$ on $z = 0$ section are shown in Fig. 10. Good agreements are found with the analytical solution [43], indicating that the present methods have relatively good performance for the three-dimensional case and non-uniform grids.

3.4. Sound generation by a circular cylinder

In previous cases, all the acoustic sources are artificial sources and the flow field is uniform. In this subsection, a realized flow-induced noise problem is presented. The flow field is first simulated by an incompressible DNS solver, with the sharp interface IBM [25], and the time-averaged flow field and acoustic sources are input into APEs. The reference lengths for both the flow and acoustic simulations are the cylinder diameter D. The Reynolds number based on cylinder diameter ($Re = U_\infty D/\nu$) is 200, and the Mach number ($Ma = U_\infty/C_\infty$) is 0.2 [22,23,29]. In the present case, the same Cartesian grid and computational domain are applied for the flow and acoustic fields. However, the two grids and computational domain can be different considering the different requirements between the flow field and acoustic simulations, and mesh interpolation is necessary under this condition. High-resolution grids are generated in the vicinity of the cylinder and in the wake to better resolve the vorticial structures in the flow. The uniform grid with $dx = dy = 0.03D$ is used around the cylinder, and the uniform mesh is also applied to resolve acoustic waves when the grid size increases to $1.4D$, which is about 18.0 PPW; the computational grids are shown in Fig. 11. The total number of grids is 512 × 512, and the computation domain is approximately $0 \le (x, y) \le 240D$. For this case, a much larger domain is designed in order to cap-

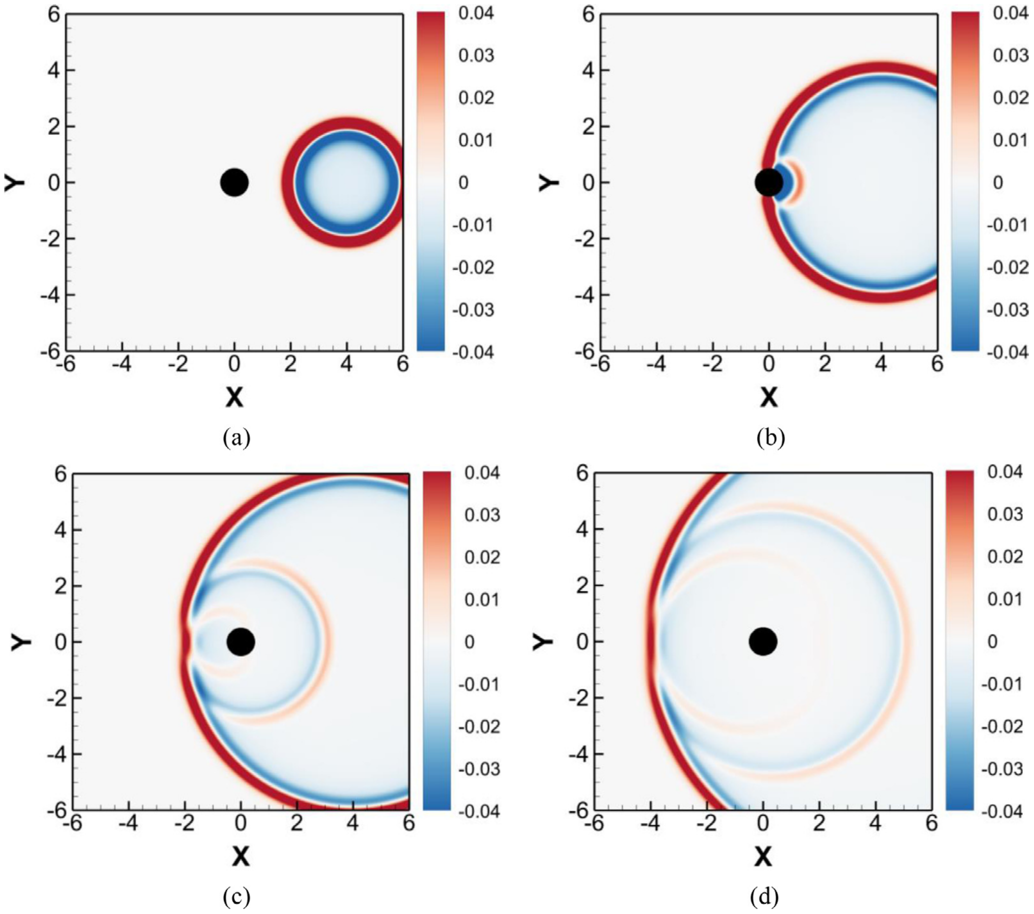

(a) (b) (c) (d)

Fig. 6. Pressure perturbation contours at (a) $t = 2$, (b) $t = 4$, (c) $t = 6$, and (d) $t = 8$.

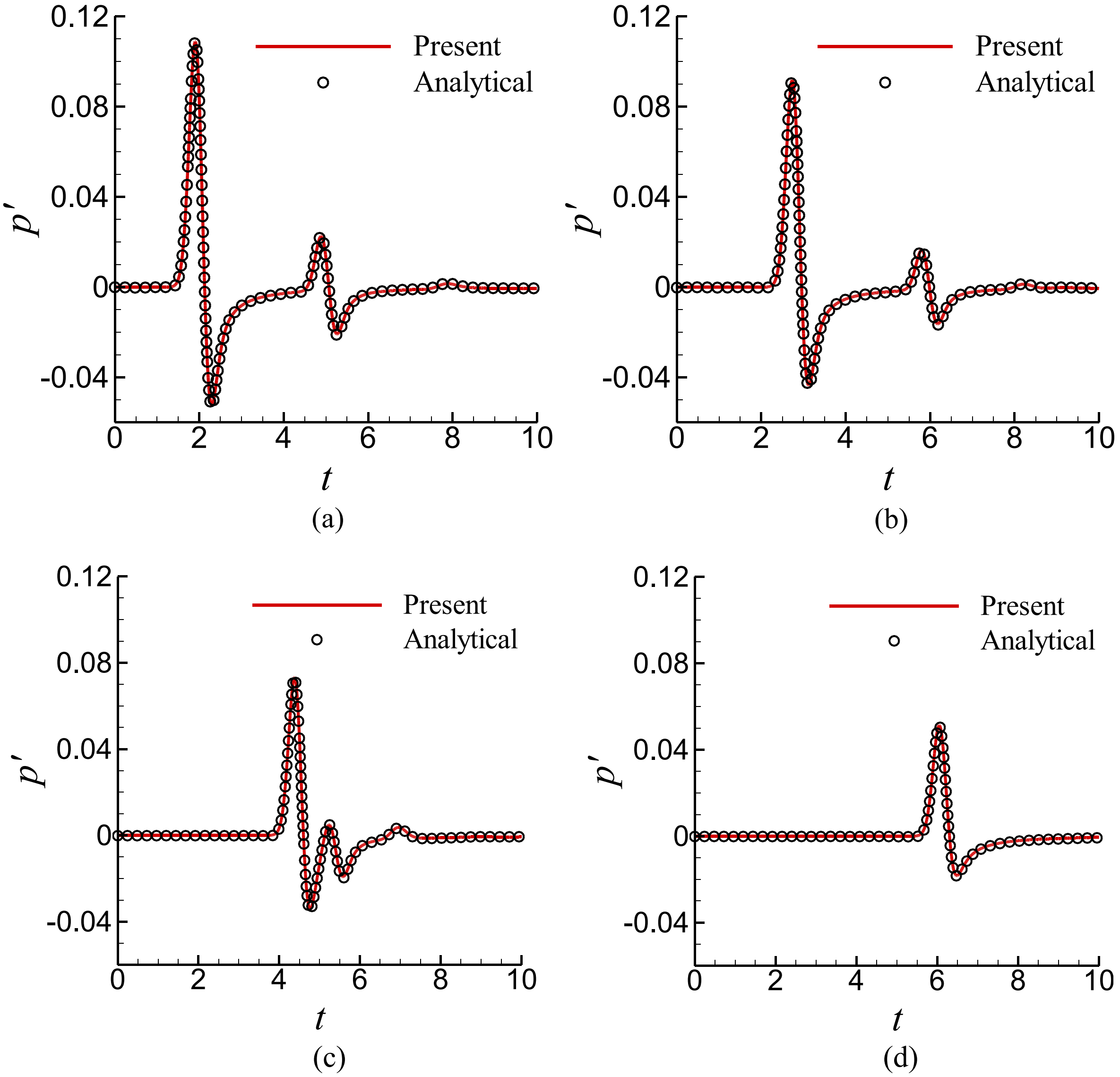

(a) (b) (c) (d)

Fig. 7. Comparison between present and analytical solutions at four positions from $t = 0$ to $t = 10$ at point: (a) A (2, 0), (b) B (2, 2), (c) C (0, 2) and (d) D (−2, 0).

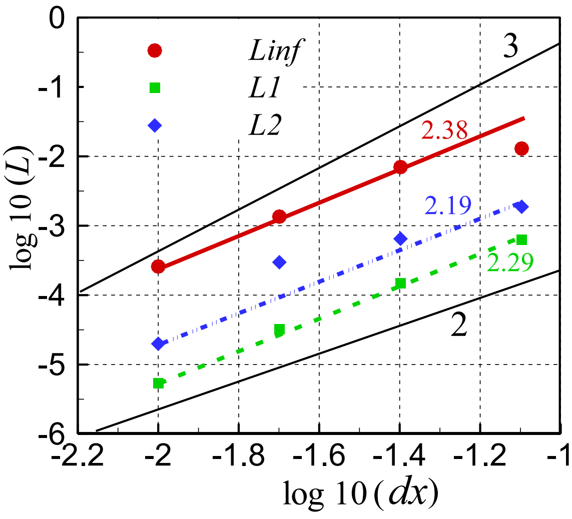

Fig. 8. Convergence curve of pressure perturbation including immersed boundary.

ture the sound in the far-field and reduce the effect of the boundary on the acoustic field. The time step of the flow simulation is $0.005D/U_\infty$, as the non-dimensional time is different for the flow field and the acoustic field; the time step for the acoustic simulation is $0.005D/C_\infty$, which is one-fifth of the time step for the flow simulation. In the low-Mach number limit where only vortex sound is considered, the major acoustic sources can be expressed as follows:

$$S_{\mathrm{cont}} = 0,$$
$$\boldsymbol{S}_{\mathrm{mom}} = \frac{\nabla P\prime}{\rho_0} = \frac{\nabla(P-\bar{P})}{\rho_0} \tag{28}$$

The time-dependent acoustic source during the acoustic simulations obtained by linear interpolation between two adjacent flow time steps.

The time histories of the drag coefficient and lift coefficient are presented in Fig. 12(a). The mean drag coefficient is about 1.284, which agrees well with the value of 1.290 obtained by Russell et al. [44]. The maximum lift coefficient of 0.65 is the same as that obtained by Rosenfeld et al. [45]. The vorticity field around the cylinder is presented in Fig. 12(b), in which the von Kármán vortex street is observed in the wake. The Strouhal number (St) is 0.187, which agrees well with the values obtained exper-

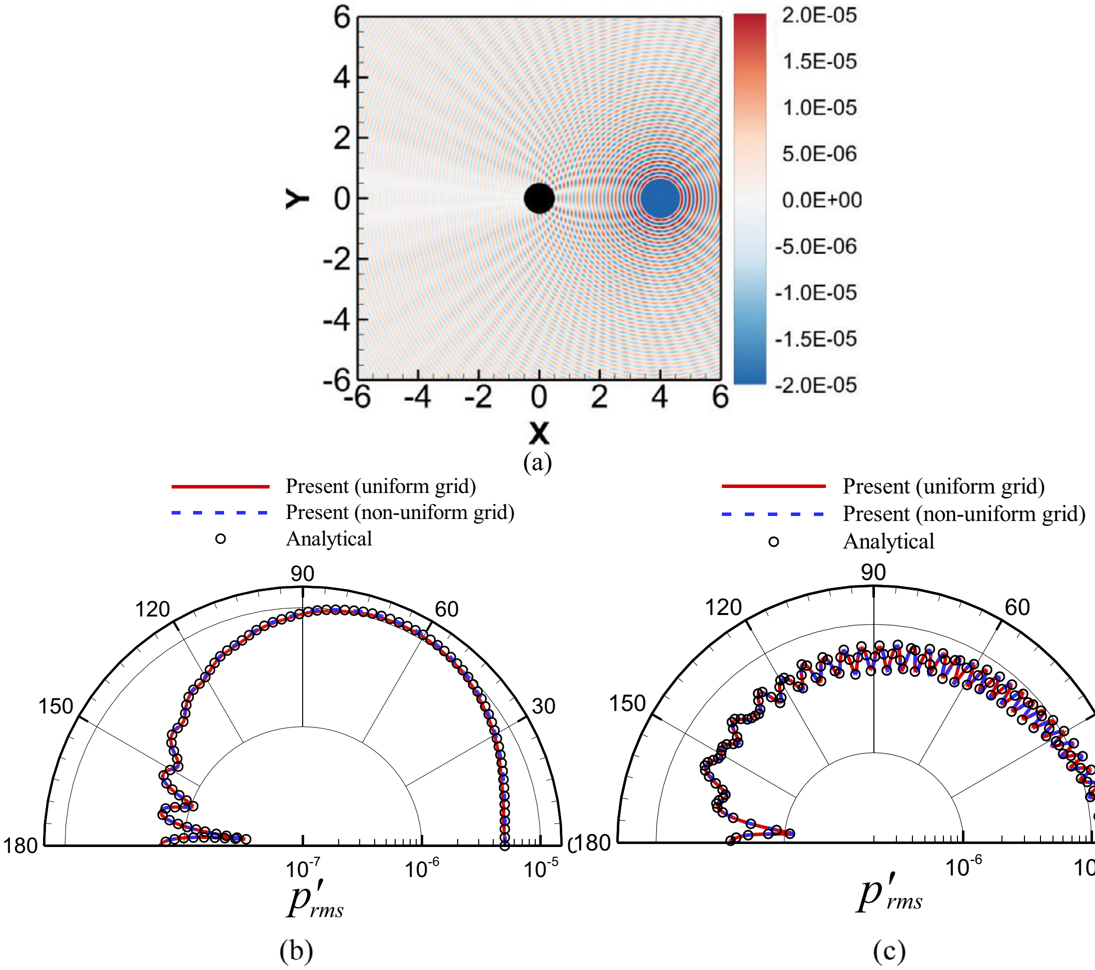

Fig. 9. Pressure perturbation contour (a) at $t = 42$ (uniform grid). Directivity patterns of analytical and present solutions at $r = 0.55$ (b) and at $r = 5.0$ (c).

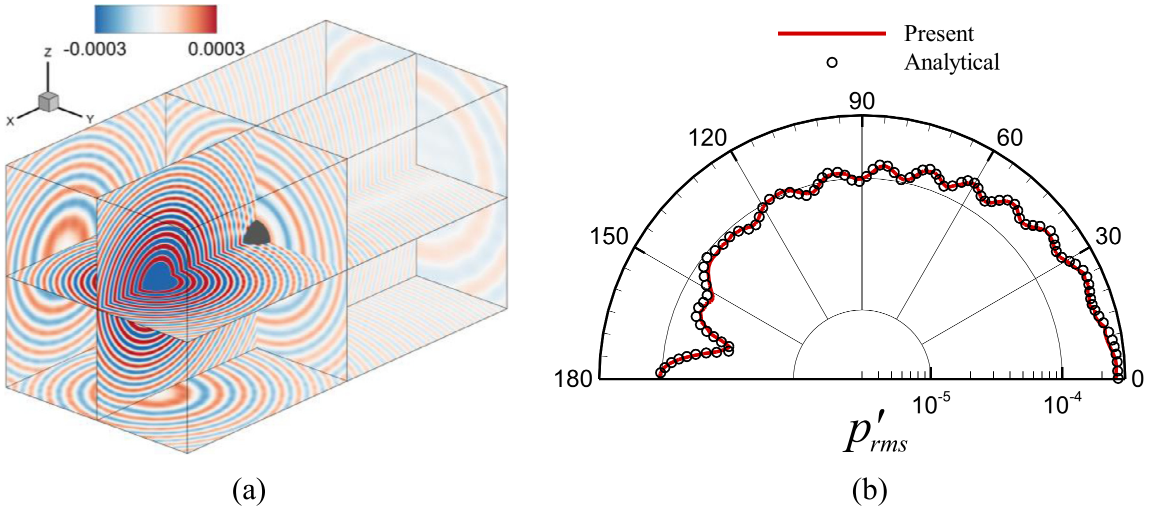

Fig. 10. (a) Pressure perturbation contour at $t = 24$. (b) Directivity pattern at $r = 2$ on $z = 0$ section.

imentally by Williamson (0.185) [46] and Le et al. [47] (0.187). The instantaneous acoustic pressure field is shown in Fig. 13(a), in which a dipole source caused by the periodic vortex shedding can be seen. In the figure, the measured non-dimensional wavelength along the y-direction is about $27D$, which is very close to the theoretically predicted value of $1/(Ma \cdot St)= 26.7D$. The pressure fluctuation along the center line ($x = 120$) above the cylinder is plotted in Fig. 13(b) and matches well with the results of Seo and Mittal [29]. The comparison between the flow field and the acoustic field demonstrates the feasibility and accuracy of the present hybrid method for dealing with flow-induced noise problems.

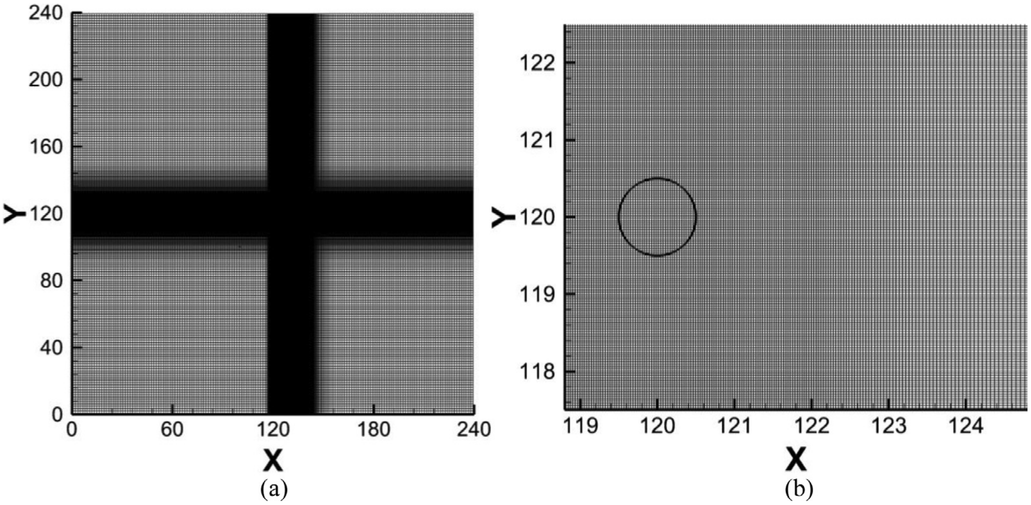
240
200
160
Y 120
80
40
0
0
60
120
180
240
X
(a)
122
121
Y 120
119
118
119
120
121
122
123
124
X
(b)

Fig. 11. (a) Computational grids of flow and acoustic simulation. (b) Densified grids around the cylinder.

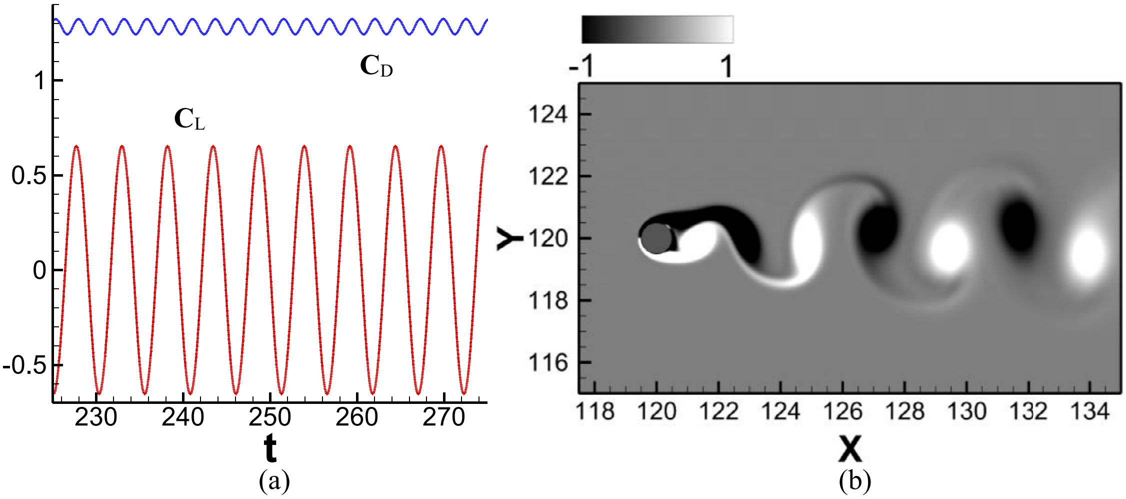

Fig. 12. (a) Time histories of drag and lift coefficient. (b) The vorticity field of the flow.

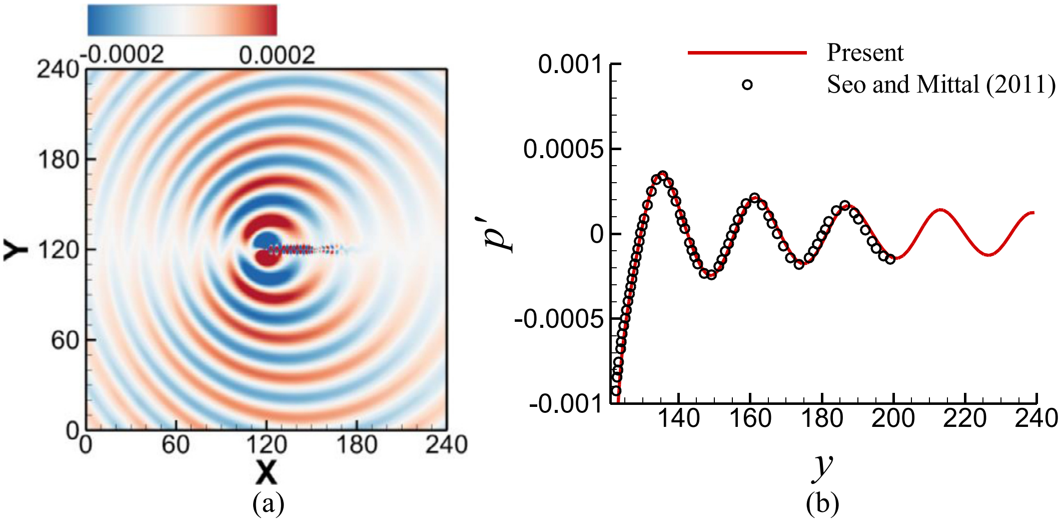

Fig. 13. (a) Instantaneous acoustic field. (b) Pressure fluctuation along the center line above the cylinder (line: present, dot: Seo and Mittal [29]).

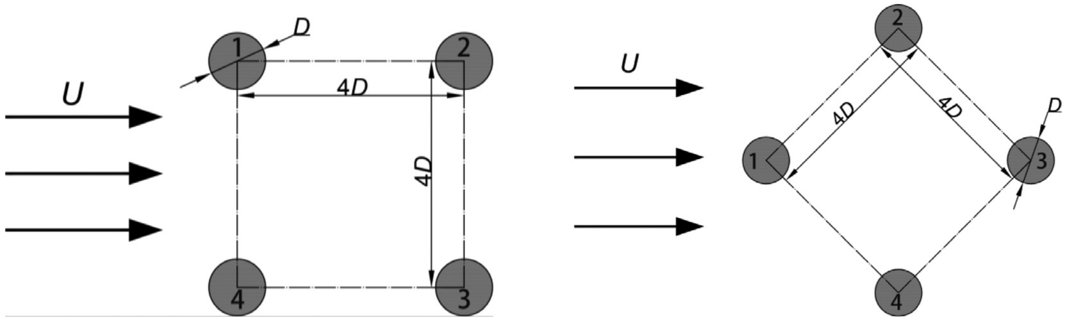

(a) (b)

Fig. 14. The schematic layouts of the array (a) square arrangement, (b) diamond arrangement.

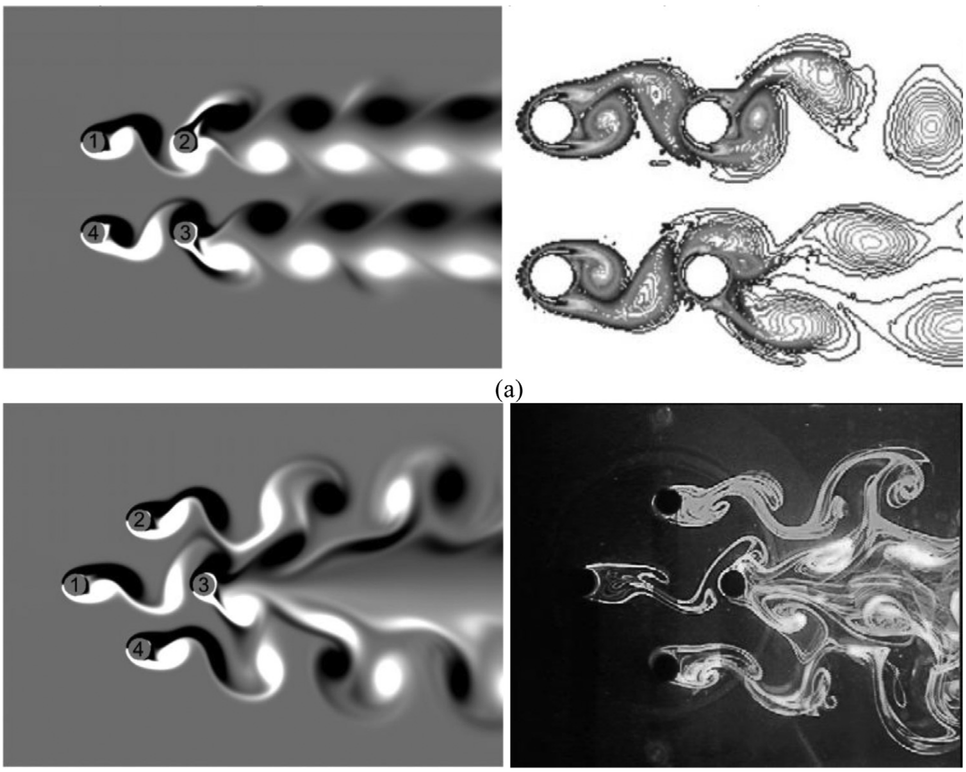

(a)

(b)

Fig. 15. Comparison of instantaneous flow field around two kinds of four-cylinder array: (a) vorticity by present method (left) and Lam et al. (simulation, right, reprinted with permission from [49]) for SA; (b) vorticity by present method (left) and flow visualization by Lam et al. (experiment, right, reprinted with permission from [48]) for DA.

3.5. *Sound generation by a four-cylinder array*

Flow past multiple cylinders is a very common phenomenon in engineering applications, for example, in the landing gear of airplanes, offshore platforms, bridge piers, and heat exchangers. There are flow interactions of adjacent cylinders, and these affect the flow patterns and the acoustic field around the structures at different arrangements. The typical flow fields of cylinder arrays have been investigated in previous experimental and computational studies [48-53]. However, the acoustic field characteristics of such arrays remain unclear. In this subsection, the sound generation by a four-cylinder array is simulated to demonstrate the ability of the present method to deal with complex geometry problems, and, furthermore, the acoustic characteristics of the models are explored, which provides the fundamental image of the typical cases in a low-Reynolds-number flow regime. Two basic types of array arrangement are investigated—the square arrangement (SA) and the diamond arrangement (DA)—as shown in Fig. 14. The diameter of the cylinder is D and the distance between adjacent cylinders is $L = 4D$. The two layouts have the same four-cylinder distribution but have angles of attack that differ by 90° The boundary conditions and incoming flow parameters are the same as in the single-cylinder case in the previous section, where the free-stream Mach number is 0.2 and the Reynolds number ($Re = U_\infty D/\nu$) is 200. The computation domain is approximately $0 \le (x, y) \le 240D$, and the total number of grids is 640 × 640 with 260 × 324 uniform grids near the cylinder array. The time steps of the cylinder array are $0.005D/U_\infty$ and $0.005D/C_\infty$ for flow field and acoustic field, respectively.

The instantaneous vorticity fields of the two arrays and their comparisons with existing results are presented in Fig. 15. The flow patterns of the two configurations are significantly different.

For the SA, the free shear layers of the two upstream cylinders (cylinders 1 and 4) are well-developed, and the shedding vortices

Table 4
Comparison of simulation results for the flow over a four-cylinder array, $Re = 200$.

Square array	Diamond array						
	Lam et al. [49]	Gao et al.[52]	Han et al.[53]	Present study	Lin et al. [51]	Han et al.[53]	Present study
$\bar{C}_{D1}$	1.413	1.304	1.318	1.154	1.273	1.191	1.073
$\bar{C}_{D2}$	0.482	0.466	0.500	0.471	1.543	1.382	1.212
$\bar{C}_{D3}$	0.785	0.883	0.500	0.471	0.602	0.547	0.464
$\bar{C}_{D4}$	1.449	1.293	1.318	1.154	1.543	1.382	1.216
$\bar{C}_{L1}$	0.081	0.080	––	0.080	0.001	––	0.008
$\bar{C}_{L2}$	0.050	0.037	––	0.038	0.048	––	0.046
$\bar{C}_{L3}$	−0.080	0.022	––	−0.038	−0.013	––	−0.01
$\bar{C}_{L4}$	−0.100	−0.074	––	−0.080	−0.048	––	−0.051
St_1	0.189	0.186	0.186	0.173	0.200	0.195	0.187
St_2	0.190	0.187	0.186	0.173	0.200	0.195	0.187
St_3	0.189	0.177	0.186	0.173	0.200	0.195	0.187
St_4	0.190	0.177	0.186	0.173	0.200	0.195	0.187

impinge on the downstream cylinders (cylinders 2 and 3); this phenomenon is called the vortex shedding flow pattern in reference [49], which featured that there is little interaction between the flow around the two pairs of tandem cylinders (cylinders 1 and 2 and cylinders 3 and 4). This flow pattern is slightly different from the typical von Kármán vortex street produced by a single cylinder. Note that the flow patterns of the SA computed using the present method and those computed by Lam et al. [49] are different from the flow patterns obtained experimentally [48,49] due to the effect of strong three-dimensional characteristics in the experiment. For the DA, the wake of cylinder 1 rolls up in the gaps and impinges directly on cylinder 3 and then slides past the surface. The shear layers of cylinder 3 separate immediately when a strong upstream vortex arrives before the formation of a complete Kármán vortex, causing a wider wake with a nearly anti-symmetrical shape behind cylinder 3. Additionally, the vortex shedding of cylinders 2 and 4 becomes in-phase with the presence of the middle cylinders 1 and 3.

Table 4 presents a comparison between the main flow variables (the mean drag coefficient ($\bar{C}_D$), the mean lift coefficient ($\bar{C}_L$), and the Strouhal number (St)), of the four-cylinder arrays obtained in the present work and those obtained by other researchers [49,51-53]. Generally, the present results match well with the results reported in the literatures. However, as shown in Table 4, the value of $\bar{C}_{D3}$ shows significant differences for square array between present results (0.471) and the results (0.785) obtained by Lam et al., which could be due to the effect of a low cycle bistable wake flow behind the downstream cylinders [49]. For diamond array, Lin et al. [51] computed the flow field using a 3D model, while the present solution was computed in 2D, resulting in a larger difference. However, the differences between the present solutions and the results obtained by Han et al. [53] are relatively small.

The instantaneous acoustic pressure fields of SA and DA configurations are presented in Fig. 16.

The results show that the acoustic field of the SA is symmetric along the transverse axis of symmetry ($y = 120$), while the DA is nearly anti-symmetric about the $y = 120$ axis, which is more similar to the single-cylinder case. In general, the sound radiated by the SA acts more like a monopole source and that radiated by the DA has a dipolar nature. However, both acoustic pressure fields show differences between the upstream and downstream, which is caused by the Doppler effect. Generally, the Doppler effect affects the wavelength, acoustic pressure amplitude, and propagation angle. As the direction of the incoming flow is along the x-axis, the wavelengths for the SA and DA in the positive and negative y-directions are constant; both are equal to their theoretical wavelength based on the vortex shedding frequency, which is expressed as $1/(Ma \cdot St)$. In the downstream and upstream directions, the wavelengths of the two arrays both shift with the ratio of $(1+Ma)$ and $(1-Ma)$, $35D$ and $23D$ for the SA case and $32D$ and $22D$ for the DA case. For the pressure amplitude, the Doppler effect has similar effects on the two arrays (i.e., the acoustic pressure gets stronger in the upstream direction and weaker in the downstream direction). The direction of the main radiation lobe in the upper half plane for DA is marked by dotted line in Fig. 16(b). Large differences can be observed, which may be caused mainly by the difference in geometrical configuration compared with a single-cylinder configuration. Inoue et al. [18] noted that the propagation angle θ_p for a single cylinder is mainly affected by the Doppler effect and can be well approximated by the relation $\theta_p = \cos^{-1} Ma$, which is ± 78.5° for $Ma = 0.2$. Our results show that the pressure pulses of SA propagate in all directions, and the non-uniformity of the acoustic wave in different directions could be attributed to convective effects. Compared with the single-cylinder case, the propagation direction for the DA case is more biased to the upstream, with $\theta_p = \pm 60°$, indicating that DA significantly affects the propagation angle.

The time history of acoustic pressure at monitoring point P_m in Fig. 16 ($x = 120$, $y = 200$) is recorded to show the acoustic characteristics of its far-field radiation. Using the fast Fourier transform (FFT), the power spectral densities (PSDs) of the acoustic pressure and the PSDs of the lift coefficients for the four cylinders in the diamond arrangement were determined and are presented in Fig. 17(a). The peak frequency of the acoustic pressure is 0.182, which is very close to its St of 0.187, indicating that the vortex-shedding and lift variation are the dominant noise sources. The PSDs of acoustic pressure for the three arrangements (i.e., square array, diamond array, and single cylinder) at monitoring points are plotted in Fig. 17(b). As shown in the figure, the dominant peaks at the monitoring point are very close between the SA, DA, and single-cylinder cases, with values of 0.173, 0.182, and 0.187, respectively. The results indicate that the peak frequency of acoustic pressure is less affected by the difference in array configuration.

The directivity patterns of the sound pressure level (SPL) for the above cases at $r = 100$ are presented in Fig. 18, where the single-cylinder case is also shown for comparison. The SPL is calculated by the following equation:

$$SPL = 20\log(p'_{\mathrm{RMS}}/p_{\mathrm{ref}})dB \tag{29}$$

where p_{ref} is 2×10^{-5} Pa in the air and p'_{RMS} is the effective sound pressure.

As shown in Fig. 18, in the single-cylinder case, a clear dipole sound source with figure-of-eight shape is observed. The results show that the curves of the two array cases are very close in the downstream directions, while there are differences in most other directions. The directivity profile of the SA is monopole-like, while the DA exhibits a more dipole-like pattern, which have been indicated as above in Fig. 16. It is noticeable that each of the ar-

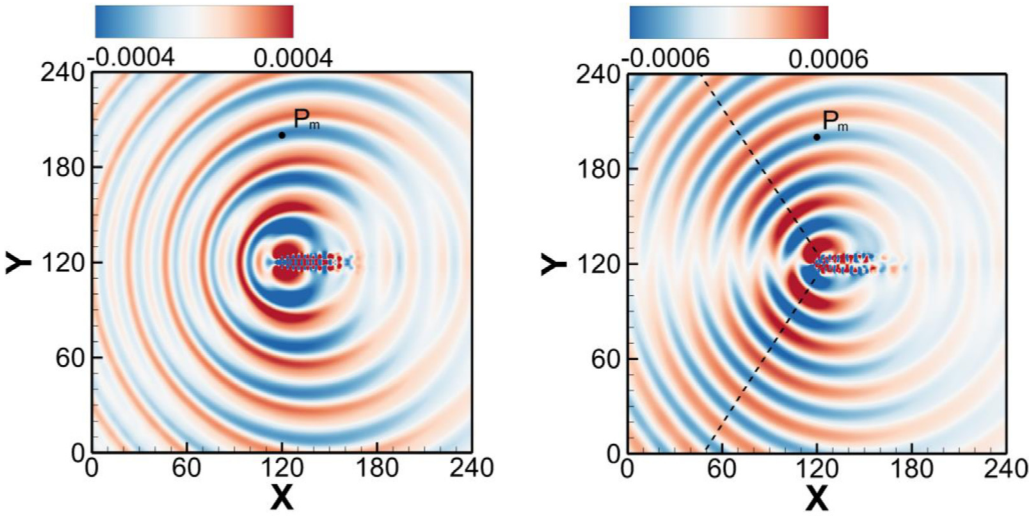

(a)

(b)

Fig. 16. Instantaneous acoustic fields of flow-induced noise of the four-cylinder (a) square array, (b) diamond array. The dotted line indicates the direction of the main radiation lobe.

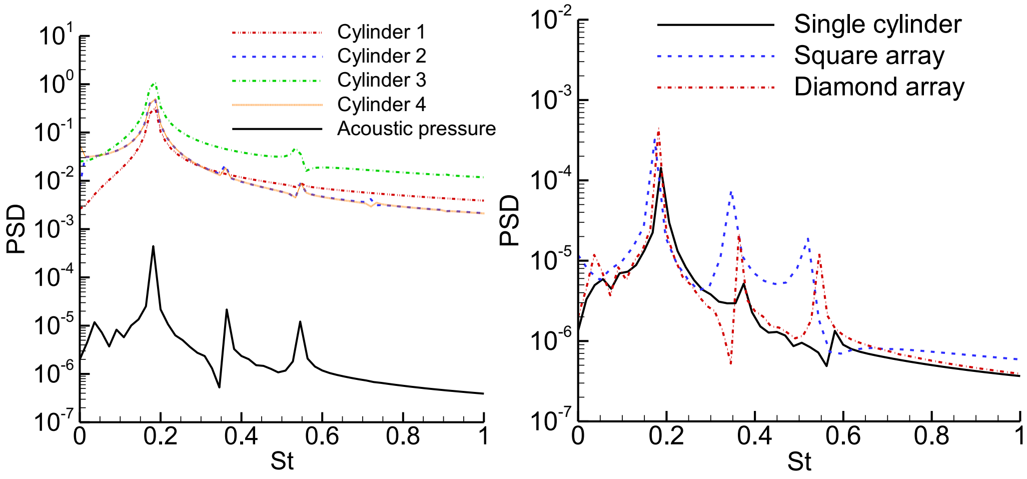

(a)

(b)

Fig. 17. (a) Power spectral densities of acoustic pressure and lift coefficients for diamond array case. (b) Power spectral densities of acoustic pressure for cases of single cylinder and cylinder arrays at point P$_m$.

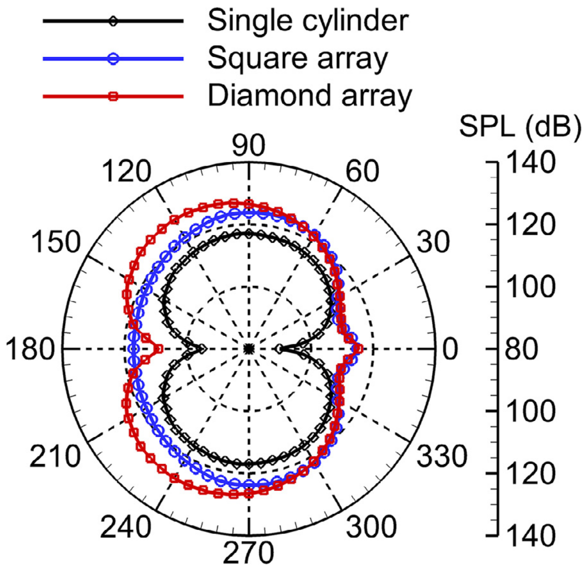

Fig. 18. Directivity patterns for single cylinder and cylinder arrays at $r = 100$.

ray cases has a visible perturbation of the lobe in the downstream direction, which does not appear for the single-cylinder case. Besides, as shown in Fig. 18, for most circumferential directions, the intensity of the generated acoustic pressure is greater for DA than SA, and those of both array cases are larger than that of the single-cylinder case. The arithmetic average values of *SPL* at circumferential observation points for the single-cylinder, square array, and diamond array cases are 106 dB, 111 dB, and 121 dB, respectively.

In this subsection, only two configurations are considered, and the distance between cylinders is constant. From our numerical experiments for two kinds of cylinder arrays, it is found that the array had a dominant influence on the acoustic field configuration. More numerical experiments involving various configurations or cylinder distances, and even moving boundary problems, will be conducted in the future.

4. Conclusions

In this paper, a unique combination of APEs and the sharp interface immersed boundary method is implemented to deal with acoustic scattering and flow-induced noise problems within a hybrid computational aero/hydroacoustic approach. An incompressible DNS solver is utilized to compute the flow field, and then the acoustic field is predicted by solving the APEs. All the equations are solved on a body non-conformal Cartesian grid, which can achieve a simple and robust algorithm for complex geometry. A series of benchmark acoustic scattering problems are used to validate the acoustic code with two- and three-dimensional problems. The present results coincide well with the analytical solutions. Furthermore, the accuracy of the proposed method is evaluated, the numerical example shows that the convergence rate of the present method with IBM is about 2.3. Then, a realized problem of noise induced by flow past a cylinder is simulated and validated. Finally, the sound generation by a four-cylinder array with two basic arrangements is investigated in detail. The following conclusions for this investigation are drawn: (1) the square and diamond arrays have monopole- and dipole-like noise shapes, respectively. In both of the two arrays, the acoustic propagation is altered by the Doppler effect, and the diamond configuration exhibits a larger propagation angle compared with the single-cylinder case; (2) the generated sound intensity of the diamond array is much greater than that of the square one in most circumferential directions, and the generated sound intensity in both of these two arrays is greater than that in the single-cylinder case; (3) the spectrums of the sound pressure level of the radiated acoustic fields for the four-cylinder arrays and the single-cylinder configuration show that they have similar profiles and peak frequencies, which indicates that they have the same mechanisms of noise generation (i.e., vortex shedding dominates the noise source generation).

Declaration of Competing Interest

The authors declare that they have no conflicts of interest to this work.

CRediT authorship contribution statement

Cheng Zhao: Methodology, Validation, Formal analysis, Writing - original draft. **Yan Yang:** Writing - review & editing, Validation. **Tao Zhang:** Conceptualization, Writing - review & editing, Supervision. **Haibo Dong:** Conceptualization, Methodology. **Guoxiang Hou:** Writing - review & editing.

Acknowledgments

This study was partially supported by ONR MURI grant N00014–14–1–0533, NSF grant CBET-1605232, and NSFC (11602277). CZ and YY are supported by the China Scholarship Council (Nos. 201806160093 and 201804910163, respectively).

References

[1] Triantafyllou MS, Triantafyllou G, Yue D. Hydrodynamics of fishlike swimming. Annu Rev Fluid Mech 2000;32:33–53.
[2] Wu TY. Fish swimming and bird/insect flight. Annu Rev Fluid Mech 2011;43:25–58.
[3] Zhang N, Zheng Z. Flow/pressure characteristics for flow over two tandem swimming fish. Comput Fluids 2009;38:1059–64.
[4] Erzincanli B, Sahin M. The numerical simulation of the wing kinematics effects on near wake topology and aerodynamic performance in hovering Drosophila flight. Comput Fluids 2015;122:90–110.
[5] Amiet RK. Noise due to turbulent flow past a trailing edge. J Sound Vib 1976;47:387–93.
[6] Dowell EH, Gorman GF, Smith DA. Acoustoelasticity: general theory, acoustic natural modes and forced response to sinusoidal excitation, including comparisons with experiment. J Sound Vib 1977;52:519–42.
[7] Sueur J, Tuck EJ, Robert D. Sound radiation around a flying fly. J Acoust Soc Am 2005;118:530–8.
[8] Bennet-Clark H, Ewing A. The wing mechanism involved in the courtship of Drosophila. J Exp Biol 1968;49:117–28.
[9] Hardin JC, Pope DS. An acoustic viscous splitting technique for computational aeroacoustics. Theor Comp Fluid Dyn 1994;6:323–40.
[10] Ewert R, Schroder W. Acoustic perturbation equations based on flow decomposition via source filtering. J Comput Phys 2003;188:365–98.
[11] Rowley CW, Colonius T, Basu AJ. On self-sustained oscillations in two-dimensional compressible flow over rectangular cavities. J Fluid Mech 2002;455:315–46.
[12] Seo JH, Moon YJ. Linearized perturbed compressible equations for low Mach number aeroacoustics. J Comput Phys 2006;218:702–19.
[13] Bailly C, Juve D. Numerical solution of acoustic propagation problems using linearized Euler equations. Aiaa J 2000;38:22–9.
[14] Wei MJ, Freund JB. A noise-controlled free shear flow. J Fluid Mech 2006;546:123–52.
[15] Lighthill MJ. On sound generated aerodynamically I. General theory. In: Proceedings of the royal society of London series A mathematical and physical sciences, 211; 1952. p. 564–87.
[16] Zhang Y, Zhang T, Ouyang H, Li T. Flow-induced noise analysis for 3D trash rack based on LES/Lighthill hybrid method. Appl Acoust 2014;79:141–52.
[17] Zhang T, Zhang Y, Ouyang H. Structural vibration and fluid-borne noise induced by turbulent flow through a 90 piping elbow with/without a guide vane. Int J Pres Ves Pip 2015;125:66–77.
[18] Inoue O, Hatakeyama N. Sound generation by a two-dimensional circular cylinder in a uniform flow. J Fluid Mech 2002;471:285–314.
[19] Bae Y, Moon YJ. On the use of Brinkman penalization method for computation of acoustic scattering from complex boundaries. Comput Fluids 2012;55:48–56.
[20] Wang M, Freund JB, Lele SK. Computational prediction of flow-generated sound. Annu Rev Fluid Mech 2006;38:483–512.
[21] Bogey C, Bailly C, Juvé D. Computation of flow noise using source terms in linearized Euler's equations. Aiaa J 2002;40:235–43.
[22] Shen WZ, Sorensen JN. Comment on the aeroacoustic formulation of Hardin and Pope. Aiaa J 1999;37:141–3.
[23] Shen WZ, Sorensen JN. Aeroacoustic modelling of low-speed flows. Theor Comp Fluid Dyn 1999;13:271–89.
[24] Ewert R, Schroder W. On the simulation of trailing edge noise with a hybrid LES/APE method. J Sound Vib 2004;270:509–24.
[25] Mittal R, Dong H, Bozkurttas M, Najjar FM, Vargas A, von Loebbecke A. A versatile sharp interface immersed boundary method for incompressible flows with complex boundaries. J Comput Phys 2008;227:4825–52.
[26] Dong H, Bozkurttas M, Mittal R, Madden P, Lauder GV. Computational modelling and analysis of the hydrodynamics of a highly deformable fish pectoral fin. J Fluid Mech 2010;645:345–73.
[27] Khalid MSU, Akhtar I, Dong H. Hydrodynamics of a tandem fish school with asynchronous undulation of individuals. J Fluids Struct 2016;66:19–35.
[28] Liu G, Ren Y, Dong H, Akanyeti O, Liao JC, Lauder GV. Computational analysis of vortex dynamics and performance enhancement due to body–fin and fin–fin interactions in fish-like locomotion. J Fluid Mech 2017;829:65–88.
[29] Seo JH, Mittal R. A high-order immersed boundary method for acoustic wave scattering and low-Mach number flow-induced sound in complex geometries. J Comput Phys 2011;230:1000–19.
[30] Geng B, Xue Q, Zheng X, Liu G, Ren Y, Dong H. The effect of wing flexibility on sound generation of flapping wings. Bioinspir Biomim 2017;13:016010.
[31] Xie F, Qu Y, Islam MA, Meng G. A sharp-interface Cartesian grid method for time-domain acoustic scattering from complex geometries. Comput fluids; 2020.
[32] Fukushima Y, Sasaki D, Nakahashi K. Cartesian mesh linearized Euler equations solver for aeroacoustic problems around full aircraft. Int J Aerospace Eng 2015;2015.
[33] Dhamankar NS, Blaisdell GA, Lyrintzis AS. Implementation of a sharp immersed boundary method in a 3-D multi-block large eddy simulation tool for jet aeroacoustics. In: 53rd AIAA aerospace sciences meeting; 2015. p. 0504.
[34] Tam CKW, Webb JC. Dispersion-relation-preserving finite difference schemes for computational acoustics. J Comput Phys 1993;107:262–81.
[35] Hu FQ, Hussaini MY, Manthey JL. Low-dissipation and low-dispersion runge–kutta schemes for computational acoustics. J Comput Phys 1996;124:177–91.
[36] Tam CKW. Computational aeroacoustics - issues and methods. Aiaa J 1995;33:1788–96.
[37] Bogey C, Bailly C. A family of low dispersive and low dissipative explicit schemes for flow and noise computations. J Comput Phys 2004;194:194–214.
[38] Vasilyev OV, Lund TS, Moin P. A general class of commutative filters for LES in complex geometries. J Comput Phys 1998;146:82–104.
[39] Tam CKW, Dong Z. Radiation and outflow boundary conditions for direct computation of acoustic and flow disturbances in a nonuniform mean flow. J Comput Acoust 1996;4:175–201.
[40] Bogey C, Bailly C. Three-dimensional non-reflective boundary conditions for acoustic simulations: far field formulation and validation test cases. Acta Acust United Ac 2002;88:463–71.
[41] Hardin J, Ristorcelli J, Tam C. ICASE/LaRC workshop on benchmark problems in computational aeroacoustics. National Aeronautics and Space Administration; 1994.
[42] Tam CK, Hardin JC. Second computational aeroacoustics (CAA) workshop on benchmark problems. National Aeronautics and Space Administration; 1997.
[43] Morris PJ. Scattering of sound from a spatially distributed, spherically symmetric source by a sphere. J Acoust Soc Am 1995;98:3536–9.
[44] Russell D, Wang ZJ. A Cartesian grid method for modeling multiple moving objects in 2D incompressible viscous flow. J Comput Phys 2003;191:177–205.
[45] Rosenfeld M, Kwak D, Vinokur M. A fractional step solution method for the un-

steady incompressible Navier-Stokes equations in generalized coordinate systems. J Comput Phys 1991;94:102–37.

[46] Williamson CH. Vortex dynamics in the cylinder wake. Annu Rev Fluid Mech 1996;28:477–539.

[47] Le Dd-V, Khoo BC, Peraire J. An immersed interface method for viscous incompressible flows involving rigid and flexible boundaries. J Comput Phys 2006;220:109–38.

[48] Lam K, Li J, Chan K, So R. Flow pattern and velocity field distribution of cross-flow around four cylinders in a square configuration at a low Reynolds number. J Fluids Struct 2003;17:665–79.

[49] Lam K, Gong W, So R. Numerical simulation of cross-flow around four cylinders in an in-line square configuration. J Fluids Struct 2008;24:34–57.

[50] Farrant T, Tan M, Price W. A cell boundary element method applied to laminar vortex-shedding from arrays of cylinders in various arrangements. J Fluids Struct 2000;14:375–402.

[51] Zou L, Lin Y-f, Lu H. Flow patterns and force characteristics of laminar flow past four cylinders in diamond arrangement. J Hydrodyn 2011;23:55–64.

[52] Y-y Gao, C-s Yin, H-q Zhang, Yang K, X-z Zhao, Sun Z. Numerical study on flow around four square-arranged cylinders at low Reynolds numbers. Math Probl Eng 2017;2017.

[53] Han Z, Zhou D, Gui X, Tu J. Numerical study of flow past four square-arranged cylinders using spectral element method. Comput Fluids 2013;84:100–12.